Chaotic map models of soot fluctuations in turbulent diffusion flames

S. Mukerji[a], J. M. McDonough[a],*, M. P. Mengüç[a], S. Manickavasagam[a],
S. Chung[b],†

[a] *Department of Mechanical Engineering, University of Kentucky, Lexington, KY 40506-0108, U.S.A.*
[b] *Department of Chemical Engineering, University of Illinois, Urbana-Champaign, IL 61801-3792, U.S.A.*

Abstract

In this paper, we introduce a methodology to characterize time-dependent soot volume fraction fluctuations in turbulent diffusion flames via chaotic maps. The approach is based on the hypothesis that fluctuations of properties in turbulent flames are deterministic in nature, rather than statistical. Our objective is to develop models of these fluctuations to be used in comprehensive algorithms to study the nature of turbulent flames and the interaction of turbulence with radiation. To this end we measured the time series of soot scattering coefficient in an ethylene diffusion flame from light scattering experiments and fit these data to linear combinations of chaotic maps of the unit interval. Both time series and power spectra can be modeled with reasonable accuracy in this way. © 1998 Elsevier Science Ltd. All rights reserved.

1. Introduction

Most practical flames are turbulent in nature. They dissipate their energy predominantly via radiative transfer. These two physical phenomena, along with chemical kinetics and soot formation, need to be understood very well for better control of flames. The nature of each one of these physical mechanisms is very complicated and more importantly, all are coupled. Yet, most of the studies performed over the years have treated each of these independently, and have not considered the interactions among them in detail.

Turbulent fluid flow is still not well understood, and radiation transfer is too complicated to be modeled in detail. Furthermore, even if a detailed model is developed, the accuracy of predictions is questionable unless the medium properties are available. These properties, e.g. soot agglomerate size, structure and volume fraction distributions, cannot be predicted with confidence without modeling the interaction of chemical kinetics, turbulence and radiation transfer. In this paper we will outline a formalism with the potential for treating interactions of these phenomena in a computationally efficient, yet realistic manner.

Detailed discussion of radiation–turbulence interactions in flames is available in the literature in the context of classical Reynolds-averaged-based turbulence models (see e.g., [2]–[7]). Despite the importance of radiation–turbulence interactions throughout the field of combustion, the problem remains "unsolved" in the sense that it is currently not possible to predict flow and heat transfer in high-Reynolds number (*Re*) combusting systems of practical importance with any degree of confidence. It must first be admitted that modeling of turbulent flows has generally been less than successful in the context of the Reynolds-averaged Navier–Stokes (N.–S.) equations even in the absence of interactions with other phenomena, and even for quite simple flows, as has been recently demonstrated by Freitas [8]. Fundamental reasons for this have been given by McDonough [9].

If progress is to be made, it will probably have to be in directions different from past efforts. In particular, it is simply not possible to correctly account for time-

---

* Corresponding author. Tel.: 001 606 257 5164; Fax: 001 606 257 3304; E-mail: super180@ukcc.uky.edu

† Contributions of S. Chung to this study were part of research conducted at the University of Kentucky as a National Science Foundation Research Experiences for Undergraduates Fellow during the summer of 1996.

dependent interactions by using equations that merely model (time-averaged) statistics, even if these equations are highly accurate. This is easily seen by considering prediction of behavior of a flame in an intermittent, gusty flow field. Statistical analysis would be likely to predict preservation of a steady combustion process at some level, whereas the physics of the situation would dictate that sooner or later the flame would be extinguished by a gust, and thereafter there would no combustion. In light of the obvious importance of understanding and thus being able to control combustion processes, and the fact that past radiation–turbulence interaction analyses have been only partially successful, we have begun studies that represent a distinct departure from more standard modeling techniques.

A new technique, related to chaotic-map models, was theoretically analyzed by Hylin and McDonough [10] in the context of a turbulent modeling procedure known as additive turbulence decomposition (ATD), and the basic ideas associated with the type of model employed have been considered previously in a somewhat ad hoc way by, e.g., Sreenivasan and Ramshankar [11]. The overall ATD procedure consists of solving large-scale, unaveraged governing equations containing small-scale dependent variables that are directly modeled or simulated in some manner closely resembling large eddy simulation (LES). It is important to recognize that this represents a significant departure from the usual Reynolds-averaged methods in which statistics, i.e., correlations of dependent variables, are modeled. It is this feature of modeling physical aspects of the flow that leads to the ability to directly model interactions of turbulence with other phenomena, but at the same time it raises new issues regarding construction of the required models. Methods for carrying out such constructions, and results obtained in a specific case, namely turbulent, radiating flow in a diffusion flame, will be the subject of this paper.

We will present a modeling approach to account for interactions of turbulence with radiation and specifically focus attention on the problem of introducing features of physical measurements into the models. In a recent study [1] a detailed experimental approach was outlined to measure the soot volume fraction fluctuations in a turbulent flame, which were later correlated using chaotic-map models. Even though the results presented [1] are quite promising, the need for more thorough analysis is obvious. A detailed description of the map construction procedure, per se, in the context of a model problem is presented by McDonough et al. [12].

The key underlying idea is to employ one-dimensional chaotic maps of the unit interval as the foundation for the model [13]. The rationale behind this stems from the 'universality' properties of certain of such maps, as demonstrated by Feigenbaum [14], and others, and particularly from the fact that their bifurcation sequences can be similar to those of the N.–S. equations [15]. (A non-rigorous plausibility argument for this is given by Frisch [16].) Thus, they appear to provide good candidates for models of fluctuating variables associated with fluid flow and related transport phenomena.

Here, we focus only on the use of chaotic maps for quantification of soot mass fluctuations in turbulent diffusion flames. Soot volume fraction plays a major role in radiation–turbulence interactions in flames. In general, soot formation and oxidation processes are controlled by the chemical kinetics, which is a strong function of temperature and species concentration gradients. Both of these gradients are affected by the structure of the turbulent flow field and by strong radiative heating and/or cooling. It will be shown via analysis of experimental results that the radiation–turbulence interactions in sooting diffusion flames can be deterministic in nature, thus motivating the approach being employed here. The main results of this paper are the following: (i) a formalism for radiation–turbulence models based on dynamical systems theory, and (ii) construction, analysis and comparison with experimental data of such a model specifically for soot volume fraction fluctuations.

2. Chaotic-map models

In this section we will provide details of the approach taken to derive the new types of models described in the Introduction. We begin with a brief outline of the ATD formalism to indicate precisely how such models can be used in the framework of unaveraged governing equations for fluid flow, heat transfer, etc., and thus to provide a rationale for modeling requirements. We then briefly describe the laboratory experiments employed to obtain data for the present study. The reader is refered to [1] for a more complete treatment of the experimental aspects.

2.1. Additive turbulent decomposition

The modeling procedure we employ here has evolved from early work by McDonough et al. [17, 18] and McDonough and Bywater [19, 20] on 'large-scale/small-scale decomposition' approaches applied to the Burgers' equation model of the N.–S. equations. Additive turbulent decomposition is now viewed as a family of methods ranging from highly-parallelizable direct numerical simulations (DNS)(cf. McDonough and Wang [21] and Mukerji and McDonough [22]) to the very efficient modeling procedures introduced in [10], and employed in McDonough et al. [23, 24] and Salazar et al. [25]. It is this latter form of ATD to which the present chaotic map construction pertains.

The ATD formalism consists of unaveraged, time-dependent transport equations along with an additive decomposition of both the dependent variables (as in large-eddy simulation) and of the governing equations

themselves. We note that the nonlinear Galerkin (NLG) procedures of Temam and various co-workers (e.g. Marion and Temam [26]) comprise a special case of ATD, as is clear from recent work of Brown et al. [27]. If we let **q** denote the dependent variable vector, then in the above context we can write

$$\mathbf{q}(\mathbf{x}, t) = \sum_{k=1}^{K} \mathbf{q}^{(k)}(\mathbf{x}, t), \quad \mathbf{x} \in \mathbb{R}^d, \quad d = 1, 2, 3, \qquad (1)$$

where each $\mathbf{q}^{(k)}$ represents a 'scale of behavior' of the physical phenomena (or in mathematical terms, an element of a subspace of an appropriate Hilbert space), and $\mathbb{R}^d$ denotes d-dimensional Euclidean space. When $K = 2$ we have

$$\mathbf{q}(\mathbf{x}, t) = \bar{\mathbf{q}}(\mathbf{x}, t) + \mathbf{q}^*(\mathbf{x}, t), \qquad (2)$$

which is analogous to LES if we view $\bar{\mathbf{q}}$ as the 'resolved' scales and $\mathbf{q}^*$ as the 'unresolved' scales.

A typical transport equation for **q** can be expressed in the general form

$$\mathbf{q}_t + \nabla \cdot \mathbf{F}(\mathbf{q}) = \nabla \cdot \mathbf{G}(\mathbf{q}) + \mathbf{S}(\mathbf{q}), \qquad (3)$$

where **F**, **G**, and **S** are advective (nonlinear), diffusive and source terms, and the subscript t denotes differentiation with respect to time; ∇ is the gradient operator. Substitution of (2) into (3) results in

$$(\bar{\mathbf{q}} + \mathbf{q}^*)_t + \nabla \cdot \mathbf{F}(\bar{\mathbf{q}} + \mathbf{q}^*) = \nabla \cdot \mathbf{G}(\bar{\mathbf{q}} + \mathbf{q}^*) + \mathbf{S}(\bar{\mathbf{q}} + \mathbf{q}^*). \qquad (4)$$

We observe that in typical Reynolds-averaged approaches equation (4) would be averaged, whereas in 'complete' ATD it would be additively decomposed into large- and small-scale parts (see [21] for details).

In the present case we would solve equation (4) for $\bar{\mathbf{q}}$, and model $\mathbf{q}^*$. this leads to efficient computational procedures that can be applied on coarse grids (fine meshes are not needed to resolve large-scale behavior), but which are capable of predicting small-scale flow features such as transition to turbulence, relaminarization and interactions between fluid motion and other physical phenomena. It is the construction of these models, especially the fluctuating chaotic maps on which they are based, that comprises the main focus of the present work.

2.2. General form of $\mathbf{q}^*$

As implied above, we expect to solve equation (4) on relatively coarse grids (generally no finer than might be used in Reynolds-averaged method solutions) intended to accurately resolve only the large scales of motion. In particular, it should not be expected that $\bar{\mathbf{q}}$ will include any significant portion of inertial subrange scales. It follows that $\mathbf{q}^*$ must serve as a correction to this under-resolved solution approximation, and must in some sense model a significant portion of the effects of energy transfer through the inertial subrange, and the dissipation of energy at the Kolmogorov scales.

In principle there are at least several ways by which

one might accomplish this, and here we describe only the approach we believe to be the simplest. Before providing the details, however, we note a fundamental constraint that we wish to impose on any such model. Namely, we require $\mathbf{q}^* \to \mathbf{0}$ as discretization step sizes go to zero in order to preserve the consistency of equation (4) with equation (3). The obvious consequence of this is that for this class of models, the complete procedure automatically collapses to DNS. We comment that the rate at which this occurs with respect to refinement of the discretization is also very important for accuracy [10].

We must also emphasize that the quantities being modeled here are distinctly different from those modeled in Reynolds-averaged approaches and in LES: $\mathbf{q}^*$ is the vector of fluctuating dependent variables rather than statistical correlations between various combinations of these. This leads to several advantages, the most important of which are the ability to model instant-by-instant fluctuations and interactions, the significant reduction in the number of quantities requiring a model, and the ability to obtain direct laboratory measurements for all modeled quantities. The first of these addresses problems associated with highly unsteady flows alluded to in the Introduction. The second leads to greatly simplified modeling procedures; the reader is referred to Wilcox [28] to gain an appreciation for the extreme complexity of modern Reynolds-averaged-based models. This will also provide a understanding of the experimental difficulties associated with such models; viz, the models require experimental results for numerous statistical properties that cannot be measured and often cannot even be accurately deduced from measurements.

The form of the chaotic map model considered here is

$$\mathbf{q}^* = \mathbf{A}\zeta\mathbf{M}, \qquad (5)$$

where **A** is an amplitude factor constructed from classical theories of isotropic turbulence; ζ is an anisotropy correction factor consisting mainly of first-order structure functions of (local in space and time) high-pass filtered resolved-scale variables, and **M** is a vector of nonlinear (potentially chaotic) algebraic maps. The amplitude factor must account for scales of motion ranging from just smaller than the resolved scales to the Kolmogorov scales, and it may be different for different components of $\mathbf{q}^*$. The anisotropy factor must account for both physical and numerical grid anisotropies, the latter of which have proven difficult to treat in the context of LES specifically because of filtering used to obtain equations for the resolved scales. Finally, the chaotic map **M**, the main topic of the present study, must reflect the bifurcation sequences, time scales and general fluctuating character of physical variables over the appropriate (as induced by the resolved-scale calculations) range of scales. A complete analysis of equation (5) is provided in [10], and a more detailed summary than presented here (with formulas for **A** and ζ) can be found in [23]. In

neither if these references, however, is much concern given to choice of the map **M**, or to its construction from experimental data. We will address these issues in Section 3.

2.3. Experimental data

Experiments were performed using a co-flow diffusion flame burner. The burner consists of a central fuel tube surrounded by a co-annular oxidizer tube having diameters of 1 and 5 cm with an overall height of 35 cm, and has been designed to produce a flat velocity profile of the oxidizer and the fuel. The oxidizer tube has two diametrically opposed inlet ports which make possible an even distribution of the oxidizer across the cross-section of the tube. As oxidizer, pressurized bottled air was used. Ethylene (99.5% purity) was employed as fuel. A diagnostic system based on a short-pulse, 532 nm wavelength, solid-state Q-switched Nd:YAG laser with an optical parametric oscillator was utilized for data collection [1].

The underlying intent of the experiments conducted for this study is to obtain data on angularly scattered light intensity as a function of time. This variation in recorded intensity is related to transience of the scattering particles (soot) in the control volume at the focal point of the laser beam. Experiments were conducted to obtain data on scattered light intensity from soot particles at $30°$, providing a measure of soot volume fraction, f_v, as a function of time. The time-series were obtained by making single-shot measurements at the rate of thirty data points per second (i.e., at laser pulse frequency) for the ethylene flame using several different air-fuel ratios, and measurements were recorded at several different heights.

It is important to realize that similar experiments can be carried out with a continuous-wave laser modulated using an optical chopper. These types of experiments are needed to identify the effects of data collection frequency on observables. As discussed before, however, our objective here is to present a methodology rather than bringing a complete solution to the problem. For this reason we did not conduct experiments other than those performed at a single frequency of 30 Hz.

The fundamental hypothesis in our approach to analyzing these data, and subsequently constructing turbulence models, is that turbulent fluid flows and any associated interacting phenomena are deterministic, rather than stochastic, in nature. It should be noted that this hypothesis is amply supported by both theoretical and experimental results beginning with the work of Ruelle and Takens [31]. It is therefore reasonable to employ deterministic dynamical systems as turbulence models, and we remark that the N.–S. equations comprise one such system. But there exist much simpler systems possessing many of the features of the N.–S. equations,

viz., chaotic time-series and bifurcation sequences leading from steady to periodic, and on to chaotic behavior.

There are a number of important tools that have been developed for the qualitative and quantitative analysis of dynamical systems, or more precisely, for analysis of time-series generated by the evolution of such systems. The reader is referred to Guckenheimer and Holmes [32] and Bergé et al. [33] for very readable treatments. Here, we will specifically employ the following in the analysis of our experimental data: (i) time series, (ii) power spectral density (psd), (iii) delay maps, and (iv) various statistical characterizations; but we caution that use of additional ones such as Poincaré maps, correlation dimension, etc. may be necessary to obtain more refined results. Moreover, it should be emphasized that none of these quantities (i.e., power spectra, fractal dimension, etc.) can be inverted to imply a unique time series. Thus the modeling effort must employ more sophisticated analyses and quantification of the time series behavior itself, e.g., use of total variation per unit time, frequency of zero crossings, etc., in order to more precisely model complex, periodic deterministic phenomena. These latter techniques have recently been employed [12] in the context of fitting data obtained from a model problem. We will utilize several of the most effective techniques identified in that study below. Also note that in our earlier study, [1], the modeling effort was limited to fits of psd profiles.

We begin with direct observation of time series of measured data in an effort to detect general features of the temporal behavior of the phenomenon under consideration such as periodicity, intermittency or more complex behavior. Comparison of time series from different spatial locations and/or for different values of a control (bifurcation) parameter, e.g., air–fuel ratio, may reveal features suggesting a particular bifurcation sequence, and thus a particular chaotic map (or maps) to be employed as a model.

Figure 1 presents four snap-shots of the flame over a 1 s time interval. The exposure for each image is 1/4000 s. The base diameter of the flame is 1 cm. The Reynolds number of the flame is increasing with increasing height, and for the flame depicted it can be given roughly as $Re = 400\,L$, where L is the length measured from the nozzle (in cm). These Reynolds numbers are not very large; thus, the flame itself is, to an extent, in the buoyancy-influenced regime. This provides a possible explanation for observed strong oscillations at about 12 Hz, which may be due to the buoyant instability as discussed in [30]. With increasing Reynolds numbers, this instability is likely to lose its importance. Indeed, our experimental data also show that with increasing flame height, the importance of 12 Hz oscillations diminishes.

The corresponding time series and psd at several axial locations are shown in Figs 2(a–c) and 3(a–c) respectively. The time series suggest that the flow becomes more turbulent at higher axial locations (increasing Re). In

Fig. 1. Photograph of the ethylene diffusion flame at four successive time slices.

particular, these data are strongly suggestive of a subharmonic bifurcation sequence of the Feigenbaum type [14]. As will be discussed in more detail in the next section, it is possible to gain considerable information regarding time scales and amplitudes of various flow 'structures' simply through careful qualitative analysis of the time series. But if details regarding periodic, subharmonic or quasi-periodic features are required (as they are for our present purposes), it is necessary to calculate the power spectra. We comment that for turbulent, chaotic data it is typical for the psd to consist of a broadband spectrum (significant power over a wide range of frequencies) with $f^{-\alpha}$ decay, with α often in the range $0 < \alpha < 2$. The psds displayed in Fig. 3(a–c) show only a limited decay, but on the other hand there is clear evidence of a subharmonic bifurcation sequence (the 6 and 12 Hz peaks in Fig. 3(b, c)). Thus the chaotic map(s) chosen for the modeling process should at least exhibit this feature. (Here it is worth noting that the 12 Hz oscillations are in the range of those reported by Buckmaster and Peters [30]).

3. Model construction

We begin model construction by noting that the power spectra presented in Fig. 3(a–c) are very similar to those obtained from the time series of the logistic map, a widely studied nonlinear algebraic map [13]. Such strong similarities earlier motivated us to employ a slightly modified form of the logistic map,

$$m_k^{(n+1)} = b_k m_k^{(n)}(1 - |m_k^{(n)}|), \tag{6}$$

as a simple model for fluctuating absorption coefficient [24]. Here, b_k is the bifurcation parameter (analogous to Re in the N.–S. equation) and $m_k^{(n)}$ is the map iterate at the nth iteration level. Since we will be attempting to fit experimental data using a combination of maps of the form (6), we use an index k to distinguish different maps in the combination. Equation (6) has also been used in [1], [12] and [23].

Although there are strong similarities between the experimental results and those obtained from the logistic map, there are also obvious differences in detail. For the present experimental data the psds clearly show at least three distinct time scales in the spatially lower part of the flame in addition to the broad-band behavior, and a simple logistic map such as equation (6) is not able to replicate this. There are numerous means by which this may be addressed. Here we will begin with a simple linear combination of logistic maps of the form of equation (6):

$$M^* = \sum_{k=1}^{K} \alpha_k \mathscr{S}_k^{(n+1)}(\omega_k, d_k, m_k(b_k)), \tag{7}$$

where the superscript $(n+1)$ indicates an advanced iteration level. Each $m_k^{(n)}$ in equation (7) is calculated from equation (6), but with different values of b_k. These values are employed in a function, $\mathscr{S}_k^{(n)}$, defined below, and the results for each index k are weighted by α_k. The final value of the map combination at the advanced iteration is constructed by adding a 'history' term so that the complete map takes the form
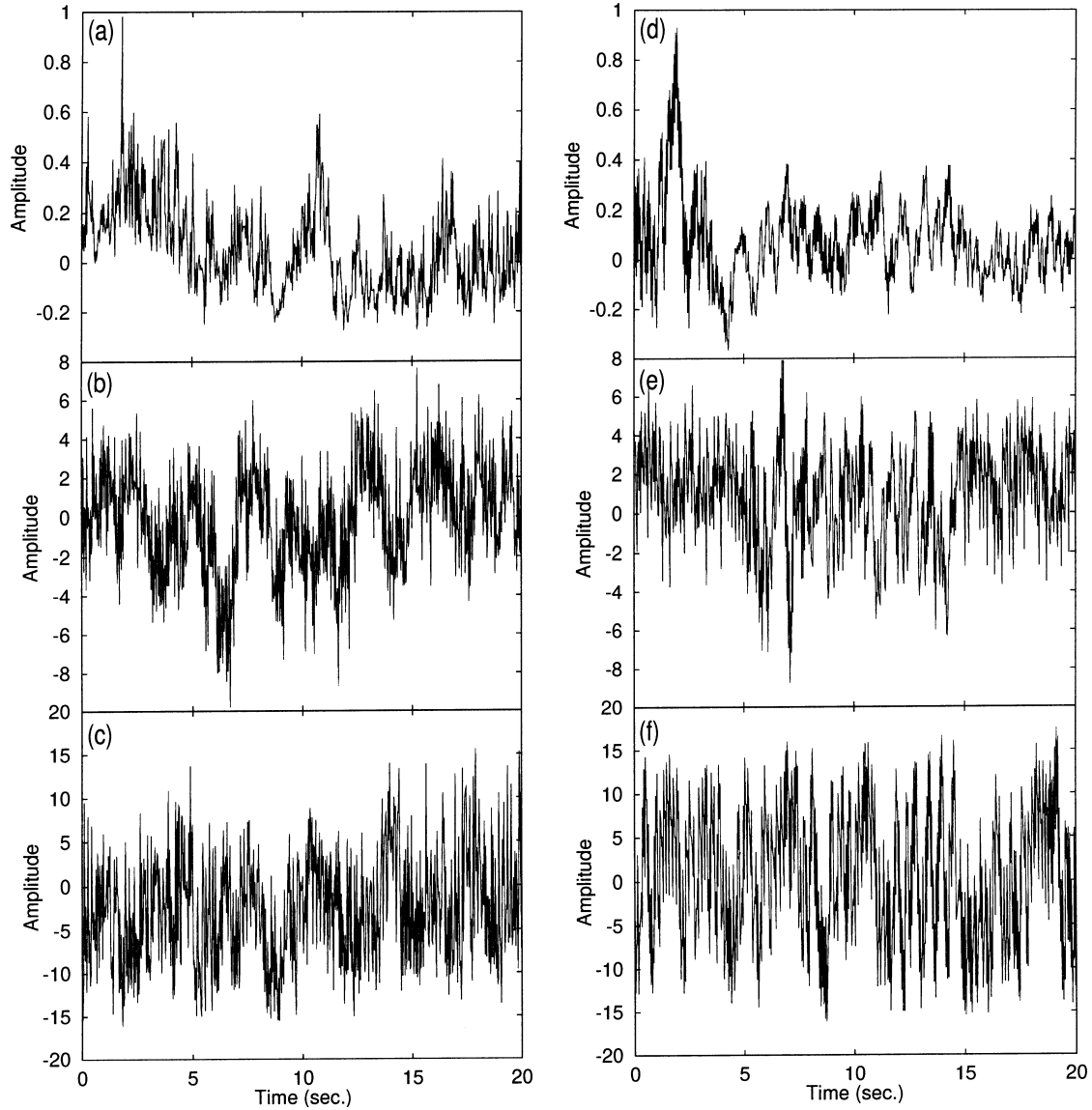
Fig. 2. Time series of scattered light intensity from soot particles at different axial locations along the flame: (a) $h = 0.5$ cm, (b) $h = 4.0$ cm and (c) $h = 7.0$ cm. Corresponding time series obtained from the best fits of linear combination of logistic maps for locations: (d) $h = 0.5$ cm, (e) $h = 4.0$ cm and (f) $h = 7.0$ cm.

$$M^{(n+1)} = \theta M^* + (1-\theta)M^{(n)}. \tag{8}$$

Here θ is an 'implicitness' factor which determines the weight assigned to the history term.

The coefficient $\mathscr{S}_k^{(n)}$ in equation (7) depends on the frequency of evaluation, ω_k, and the duration, d_k, over which each map remains active once it is switched on. This coefficient depends on a switching function, $\mathscr{F}_k^{(n)}$ and a duration function, $\mathscr{D}_k^{(n)}$. The first of these is defined as

$$\mathscr{F}_k^{(n)} \equiv \begin{cases} 1 & \text{if } (n \bmod \omega_k) = 0, \\ 0 & \text{otherwise.} \end{cases} \tag{9}$$

This determines whether the kth map is to be activated at the nth iteration. The duration function is defined as

$$\mathscr{D}_k^{(n)} \equiv \begin{cases} 1 & \text{if } \mathscr{F}_k^{(n)} = 1 \\ \mathscr{D}_k^{(n-1)} + 1 & \text{if } \mathscr{F}_k^{(n)} = 0 \text{ and } 0 < \mathscr{D}_k^{(n-1)} < d_k, \\ 0 & \text{otherwise.} \end{cases} \tag{10}$$
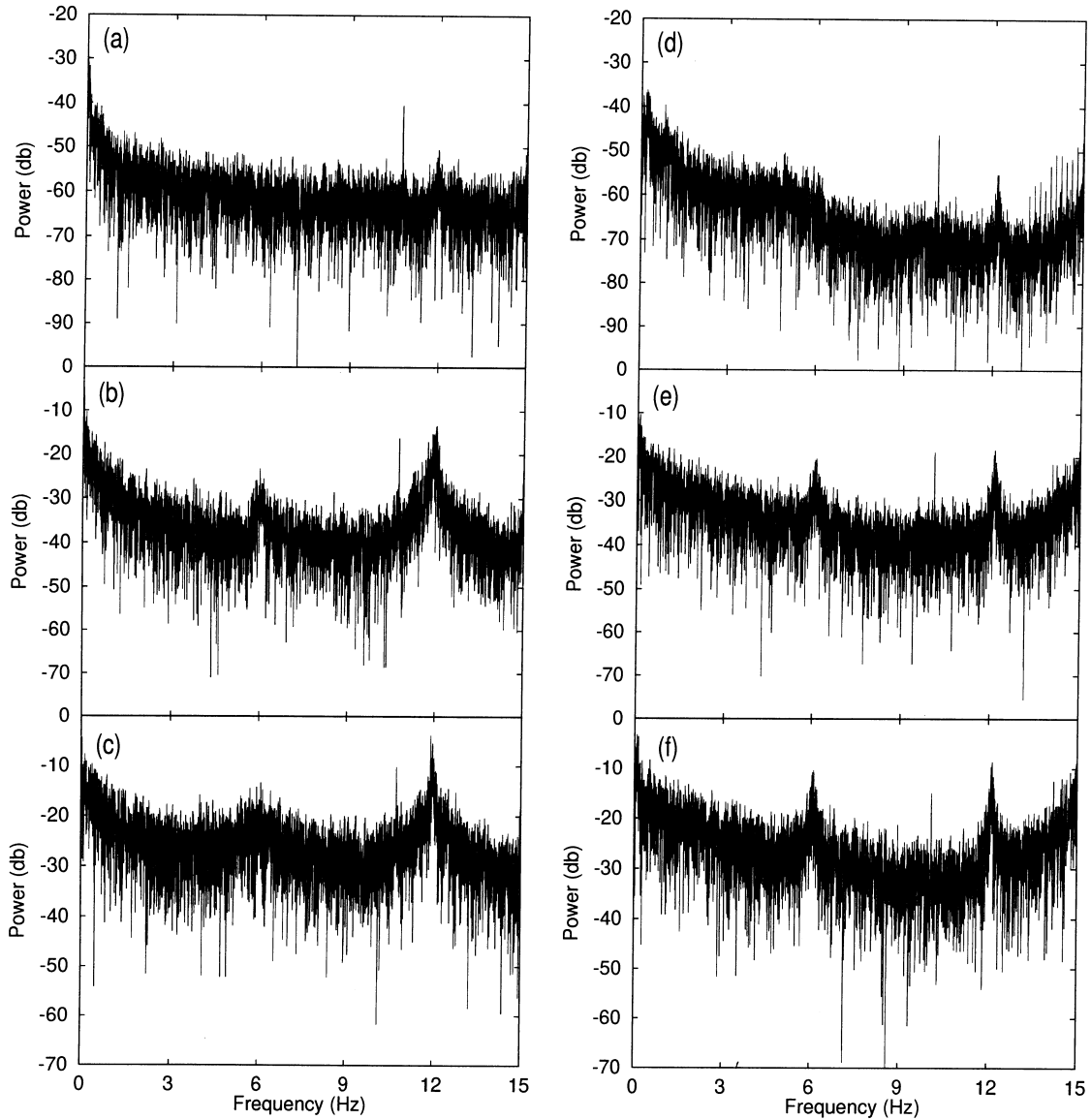
Fig. 3. Power spectra from experimental time series of soot scattering intensity at different locations: (a) $h = 0.5$ cm, (b) $h = 4.0$ cm and (c) $h = 7.0$ cm. Power spectra of time series obtained from the best fit combination of logistic maps: (d) $h = 0.5$ cm, (e) $h = 4.0$ cm and (f) $h = 7.0$ cm.

This function determines how long a map remains active. It is initialized to 1 when the map is activated according to equation (9), is incremented by 1 each time the map is evaluated and is set to 0 if it exceeds d_k. The switching function, $\mathscr{F}_k^{(n)}$, is evaluated at every iteration independent of $\mathscr{D}_k^{(n)}$. Whenever $\mathscr{F}_k^{(n)}$ is unity $\mathscr{D}_k^{(n)}$ is initialized to 1, and the kth map is (re-)activated. This happens irrespective of the current value of $\mathscr{D}_k^{(n)}$. Based on these function definitions, the coefficient $\mathscr{S}_k^{(n)}$ is computed as

$$\mathscr{S}_k^{(n)} = \begin{cases} m_k^{(n-1)} & \text{if } \mathscr{D}_k^{(n)} = 0 \\ m_k^{(n)} & \text{otherwise.} \end{cases} \quad (11)$$

Our goal in the present research is to determine b_k, α_k, ω_k and d_k so as to best fit the experimental time series with the time series obtained from the chaotic map model, $M^{(n)}$.

3.1. Data-fitting criteria

In this subsection we present one possible approach based on a least-squares minimization of differences between various properties of measured and modeled time series. We will briefly discuss the procedures suc-

cessfully used for model problem data in [12] now applied to the experimental data sets shown in Fig. 2(a–c).

The first step in this procedure is to select properties of the time series to quantify differences between measured and modeled results. We should emphasize that the set of properties employed here is not unique, but it appears to be reasonably effective. It includes both mathematical and physical characterizations: averages, total variation, L^1 and L^2 norms, slope sign changes per unit time, global minima and maxima, mean crossings per unit time, skewness, flatness, autocorrelation and 'extended' intermittency factors. We discuss each of these briefly in what follows. More details can be found in [12].

One of the most basic quantifications of a time series that should match between measured and modeled results is the time average, $\bar{u}$. But given the complicated nature of the time series shown in Fig. 2(a–c), we must refine the analysis by measuring the separate averages of the positive and negative values of u, denoted $\bar{u}^+$, and $\bar{u}^-$, respectively. The other gross quantifications of the data which we monitor are u_{max}^+, u_{min}^+, u_{max}^- and u_{min}^- the maximum and minimum of positive and negative values of u.

In addition to the averages, we also measure the average variation of the time series, an important quantification of oscillatory behavior. As was done before for the averages, we will employ separate positive and negative variations. We also measure the number of zero crossings per unit time, N_0, number of positive mean crossings, N_{mean^+} and number of negative mean crossings, N_{mean^-}, as an additional step towards matching oscillation frequencies between modeled and measured data. This can also be quantified by the number of changes in sign of the slope between successive pairs of points in the time series normalized by the total number of points, $N_{s^\pm}/N$, denoted $f_{s^\pm}$. Just as was done for variation of the time series, we can separately consider this fraction for the positive and negative parts $f_{s^\pm}^+$ and $f_{s^\pm}^-$.

The final property of the time series to be considered here that directly involves detailed oscillatory behavior is what we will term the intermittency distribution. Recall that the intermittency factor, or simply intermittency, at a point in a turbulent flow is the fraction of time during which the flow is turbulent at that point. Here we will define intermittency levels by first requiring that the segment of the time series under consideration be oscillatory, and then establishing the amplitude range of the oscillations as a fraction of the interval $[u_{min}, u_{max}]$. The number of intermittency levels employed will be specified at the time analysis of a given data set is initiated, and can be expected to change somewhat from one time series to the next. Because the intermittency distribution proved to be one of the most important measures of oscillatory behavior, and because to our knowledge it has not previously been used for analysis of experimental data, we will treat it in more detail.

To check whether a given segment of data is oscillatory we carry out the following test. At the nth discrete point we calculate the forward and backward differences,

$$\Delta_+ u^{(n)} \equiv u^{(n+1)} - u^{(n)},$$
$$\Delta_- u^{(n)} \equiv u^{(n)} - u^{(n-1)}. \tag{12}$$

If either of the following inequalities is satisfied we consider the time series to be oscillatory in a neighborhood of the nth point:

$$(\Delta_+ u^{(n)})(\Delta_- u^{(n)}) < 0,$$
$$(\Delta_+ u^{(n)})(\Delta_- u^{(n-1)}) < 0. \tag{13}$$

Once it has been established that a point is part of an oscillation it is then possible to assign it to an intermittency level. We denote the intermittency levels by I_i and the end points of these levels by g_i. Then for a total of M intermittency levels $(I_1, \ldots, I_M)$ there are $M+1$ end points $(g_0, \ldots, g_M)$ with $g_0 = u_{min}$ and $g_M = u_{max}$. The intermittency levels can now be defined in terms of g_is as:

$$I_1 = [g_0, g_1]$$
$$I_2 = [g_1, g_2]$$
$$\vdots$$
$$I_M = [g_{M-1}, g_M]. \tag{14}$$

We will denote the number of points of the time series of an intermittency level i by N_{I_i}. We can then define the intermittency factors for each level as

$$f_{I_i} = N_{I_i}/N. \tag{15}$$

The choice of M and the spacing between the g_is depends on the type of intermittency information that is critical to the analysis and has to be matched by the modeled time series.

In addition to the measures already discussed, we also calculate some global properties which may be necessary for production of accurate models. A global mathematical quantity that is widely used to characterize the 'size' of functions is the norm, $\|\cdot\|$. In this study we have employed the time averaged L^1 and L^2 norms, defined in the usual way. From a purely mathematical standpoint the L^1 norm is sometimes more appropriate, while the L^2 norm has the physical interpretation of energy.

There are additional statistical properties that are widely used in studies of turbulence, which may be appropriate quantifiers of the time series we study here. These include the autocorrelation function, the probability density function (*pdf*), the flatness F and the skewness S. The definitions for these are well known and can be found, for example, in [29].

3.2. Least-squares functional

The various measures we have discussed for quantifying the data in the form of time series will be used in the model construction process. If we let p_i^{meas} and p_i^{model}

denote the numerical value of property i as obtained from experiment and model, respectively, and define

$$\delta p_i \equiv p_i^{\text{meas}} - {}_i^{\text{model}}, \tag{16}$$

then we can define a weighted least-squares functional corresponding to N_p properties as

$$Q(\alpha, b, \omega, d) = \sum_{i=1}^{N_p} \phi_i (\delta p_i)^2, \tag{17}$$

where $\alpha = (\alpha_1, \alpha_2, \ldots, \alpha_k)^T$, etc., and ϕ_i are the weights associated with different properties. We can then determine the unknown amplitudes, bifurcation parameters, frequencies and durations of map evaluations by minimizing Q. Conceptually this is straightforward, but in practice it is difficult in the present case because the δp_i are generally not differentiable with respect to b, ω and d. Thus, direct search techniques have been used in the present study. We comment that the use of neural networks or simulated annealing techniques could be very effective in these searches, and these will be investigated in future studies.

4. Results and discussion

In this section we present results from applying the analysis techniques discussed in the preceding section to the experimental time series of scattered light intensities from soot particles obtained from laboratory experiments described in Section 2.3. The data fitting approach directly yields the parameters of the map combination which produce the best fits to the time series data at three separate axial locations along the flame. Thereafter, we use the map combination, with parameters obtained by interpolation, to predict the time series at intermediate locations in the flame. This is important because in the intended use of these maps as subgrid-scale models, we expect to specify the parameters of only a few maps at discrete spatial locations in the flow by data fitting while the parameters for maps at the intermediate locations have to be obtained by interpolation.

All results to be presented were computed in double precision (64-bit) FORTRAN on the HP-Convex Exempler SPP 1200 at the National Center for Supercomputing Applications, University of Illinois, Urbana-Champaign.

4.1. Results of data-fitting

The experimental time series at different axial locations along the flame are shown in Fig. 2(a–c). The first 5000 time steps in the time series were neglected to remove the effect of initial transients from the data. The subsequent, 10 000 time steps were used for data-fitting computations to guarantee a sufficiently long stationary state to permit reliable analyses of the sort being performed here. It should be noted that only a small segment, spanning 600

time steps, of the complete time series is shown in Fig. 2 so that salient features can be clearly identified. The corresponding power spectra and delay maps are shown in Figs. 3(a–c) and 4(a–c) respectively. The power spectrum of the experimental time series was computed using the last 8192 data points, and the delay map was constructed based on the last 2000 points with a delay of 4. The previously discussed measures for quantifying time series data were computed for each of the experimental time series of Fig. 2(a–c) and are shown in the third column of Table 1 for only the $h = 4.0$ cm axial location. These measures include intermittency factors from equation (15) in 10 equally spaced intervals, i.e. $M = 10$ in equation (14). These intermittency factors are also shown as histograms in Fig. 5(a–c).

The time series show evidence of at least three different scales of structure in both space and time, suggesting that initially we should attempt a fit with three terms ($K = 3$) in the linear combination of logistic maps in equation (7). The evidence of enhanced turbulence levels at higher axial locations is clear as the oscillation frequencies and amplitudes of the time series increase going from Fig. 2(a–c). Evidence of this increasing turbulent activity going up the flame can also be seen in the psds where the overall power levels increase from Fig. 3(a–c). But the most striking feature to be noted in the power spectra are the wide peaks at 6 Hz and 12 Hz in Fig 3(b, c). These peaks occur at lesser power levels in Fig. 3(a). This is clear evidence of a subharmonic bifurcation. Also present in each psd is a sharp peak at 10.8 Hz, possibly the result of quasi-periodicity.

Delay maps (shown in Fig. 4) seldom provide anything more than a qualitative indication of topology of a dynamical system, but they provide a simple (though not completely foolproof) indicator of deterministic, as opposed to random behavior. In this case it can be seen that the delay map of Fig. 4(c) is more 'space-filling' than that of Fig. 4(a) yielding further evidence of increased turbulent behavior.

The detailed data-fitting procedure is carried out for each of the three experimental time series shown in Fig. 2(a–c). The first step in the analyses is to set up a parameter space by choosing a wide range of combinations of values of α_k, b_k, d_k and $\omega_k, k = 1, 2, 3$. Each chaotic map combination is characterized by 12 parameters which are selected as unique permutations of values in the parameter space. The time series of the chaotic map combination is generated for each of these permutations using equations (7) and (8). The same quantifying statistics that were calculated for the experimental data are now computed for each model time series, and the least-squares functional, equation (17), is then constructed for each case. The computations for each case are independent of all others and are done in parallel. A direct search is used to identify the cases with small values of the functional, Q. These cases are considered to be the
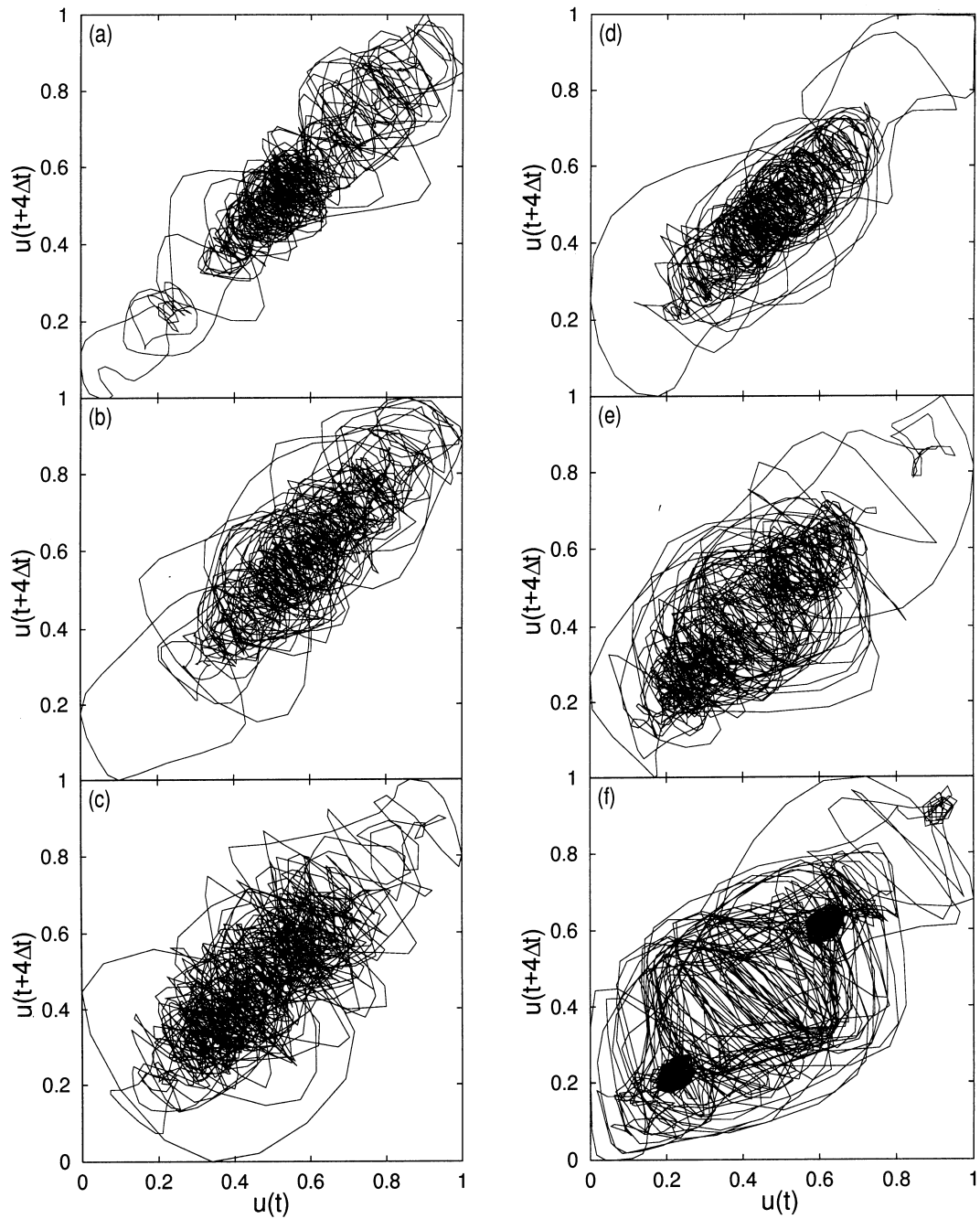
Fig. 4. Delay maps (with delay = 4) of the experimental time series of Fig. 2 at different axial locations along the flame: (a) $h = 0.5$ cm, (b) $h = 4.0$ cm and (c) $h = 7.0$ cm. Delay maps (with delay = 4) of the time series obtained from the best fit combination of logistic maps: (d) $h = 0.5$ cm, (e) $h = 4.0$ cm and (f) $h = 7.0$ cm.

'best' cases, and ten of these cases are stored in each run. These results are used to manipulate the parameter space for the subsequent runs. Initially, coarse-grained searches are made on slightly overlapping segments of the par-ameter space. Once the best segment has been identified, fine-grained searches are made on smaller subsets of this segment. This is repeated until a minimum value, Q_{min}, of the least squares functional is obtained.

Table 1
Statistical properties of data from experiments and best fit chaotic map model for location $h = 4.0$ cm in the flame

Property no. i	Description	Measured value p_i^{meas}	Modeled value p_i^{model}	Weights ϕ_i	Contribution to Q $\phi_i(\delta p_i)^2$
1	Average ($\bar{u}$)	-2.205 [-3]	-3.022 [-1]	2.296 [-6]	2.066 [-7]
2	Positive average ($\bar{u}^+$)	2.620 [0]	2.562 [0]	2.296 [-6]	7.691 [-9]
3	Negative average ($\bar{u}^-$)	-2.608 [0]	-2.863 [0]	2.296 [-6]	1.493 [-7]
4	Average variation ($\bar{V}(u)$)	3.132 [0]	3.052 [0]	2.296 [-6]	1.458 [-8]
5	Positive average variation ($\bar{V}^+(u)$)	2.553 [0]	2.099 [0]	2.296 [-6]	4.729 [-7]
6	Negative average variation ($\bar{V}^-(u)$)	2.367 [0]	2.285 [0]	2.296 [-6]	1.574 [-8]
7	Slope sign changes, total ($f_{s^\pm}$)	7.756 [-1]	7.936 [-1]	2.296 [-6]	7.440 [-10]
8	Slope sign changes, u positive ($f_{s^\pm}^+$)	7.909 [-1]	7.849 [-1]	2.296 [-6]	8.200 [-11]
9	Slope sign changes, u negative ($f_{s^\pm}^-$)	7.603 [-1]	8.013 [-1]	2.296 [-6]	3.853 [-9]
10	Time average L^1 norm	2.614 [0]	2.721 [0]	2.296 [-6]	2.628 [-8]
11	Time average L^2 norm	1.833 [-1]	1.831 [-1]	2.296 [-6]	1.792 [-13]
12	Overall minimum ($u_{\min}$)	-1.547 [1]	-1.549 [1]	2.296 [-6]	4.673 [-10]
13	Overall maximum ($u_{\max}$)	1.262 [1]	1.260 [1]	2.296 [-6]	1.513 [-9]
14	Positive minimum ($u_{\min}^+$)	1.118 [-3]	5.414 [-4]	2.296 [-6]	7.628 [-13]
15	Positive maximum ($u_{\max}^+$)	1.262 [1]	1.260 [1]	2.296 [-6]	1.513 [-9]
16	Negative minimum ($u_{\min}^-$)	-1.547 [1]	-1.549 [1]	2.296 [-6]	4.673 [-10]
17	Negative maximum ($u_{\max}^-$)	0.000 [0]	0.000 [0]	2.296 [-6]	0.000 [0]
18	Number of zero crossings/time (N_0/N)	4.158 [-1]	3.681 [-1]	2.296 [-6]	5.225 [-9]
19	Number of $\bar{u}$ crossings/time (N_{mean}/N)	4.164 [-1]	3.671 [-1]	2.296 [-6]	5.581 [-9]
20	Number of $\bar{u}^+$ crossings/time (N_{mean^+}/N)	2.920 [-1]	2.810 [-1]	2.296 [-6]	2.779 [-10]
21	Number of $\bar{u}^-$ crossings/time (N_{mean^-}/N)	2.703 [-1]	2.961 [-1]	2.296 [-6]	1.529 [-9]
22	Skewness	-1.621 [-1]	-3.558 [-1]	2.296 [-7]	8.612 [-9]
23	Flatness	3.811 [0]	2.889 [0]	2.296 [-7]	1.995 [-7]
24	Intermittency factor (f_{I_1})			5.503 [-1]	1.504 [-6]
25	Intermittency factor (f_{I_2})			1.434 [-1]	2.425 [-7]
26	Intermittency factor (f_{I_3})	Inter-	Inter-	1.122 [-2]	2.874 [-8]
27	Intermittency factor (f_{I_4})	mittency	mittency	4.656 [-4]	5.937 [-7]
28	Intermittency factor (f_{I_5})	factors	factors	4.410 [-5]	7.059 [-12]
29	Intermittency factor (f_{I_6})	shown	shown	2.075 [-5]	4.985 [-8]
30	Intermittency factor (f_{I_7})	graphically	graphically	4.326 [-5]	2.244 [-9]
31	Intermittency factor (f_{I_8})	in Fig. 5(b)	in Fig. 5(e)	3.649 [-4]	3.650 [-10]
32	Intermittency factor (f_{I_9})			9.309 [-3]	8.583 [-7]
33	Intermittency factor ($f_{I_{10}}$)			3.148 [-1]	6.172 [-7]

Least squares functional, $Q = 5.016$ [-6]. Maximum contribution to Q is from property 24, f_{I_1}.

The direct search was carried out according to the strategy described above. Map combinations involving 3 and 4 terms were tried, i.e., $K = 3$ and $K = 4$ in equation (7). It was found that a combination of four maps produced Q values at least an order of magnitude smaller than the fits with three maps. Hence only the four map combination has been used in the present study to obtain all the results discussed below. The map parameters corresponding to the best case for each location in the flame are given in Table 2. It can be seen from this table that the four bifurcation parameters, b_k, of the map combination, do not change with fits to different locations in the flame. The iteration frequencies, ω_k, also do not

change; but some slight changes are observed in the duration counts, d_k. Most of the changes occur in the amplitude factors, α_k. From our experience in this research, the b_k had the strongest influence on $Q_{\min}$. But, the particular combination of b_k shown in Table 2 turns out to be surprisingly stable with respect to data fits at different flame locations.

The implicitness factor, θ, was not a part of the direct search but was manually modified as the search progressed, and its optimal value is also shown in Table 2. From equation (8) it can be seen that larger values of θ, imply less 'memory' of a time series of its past behavior. The monotonically increasing trend of θ (from Table
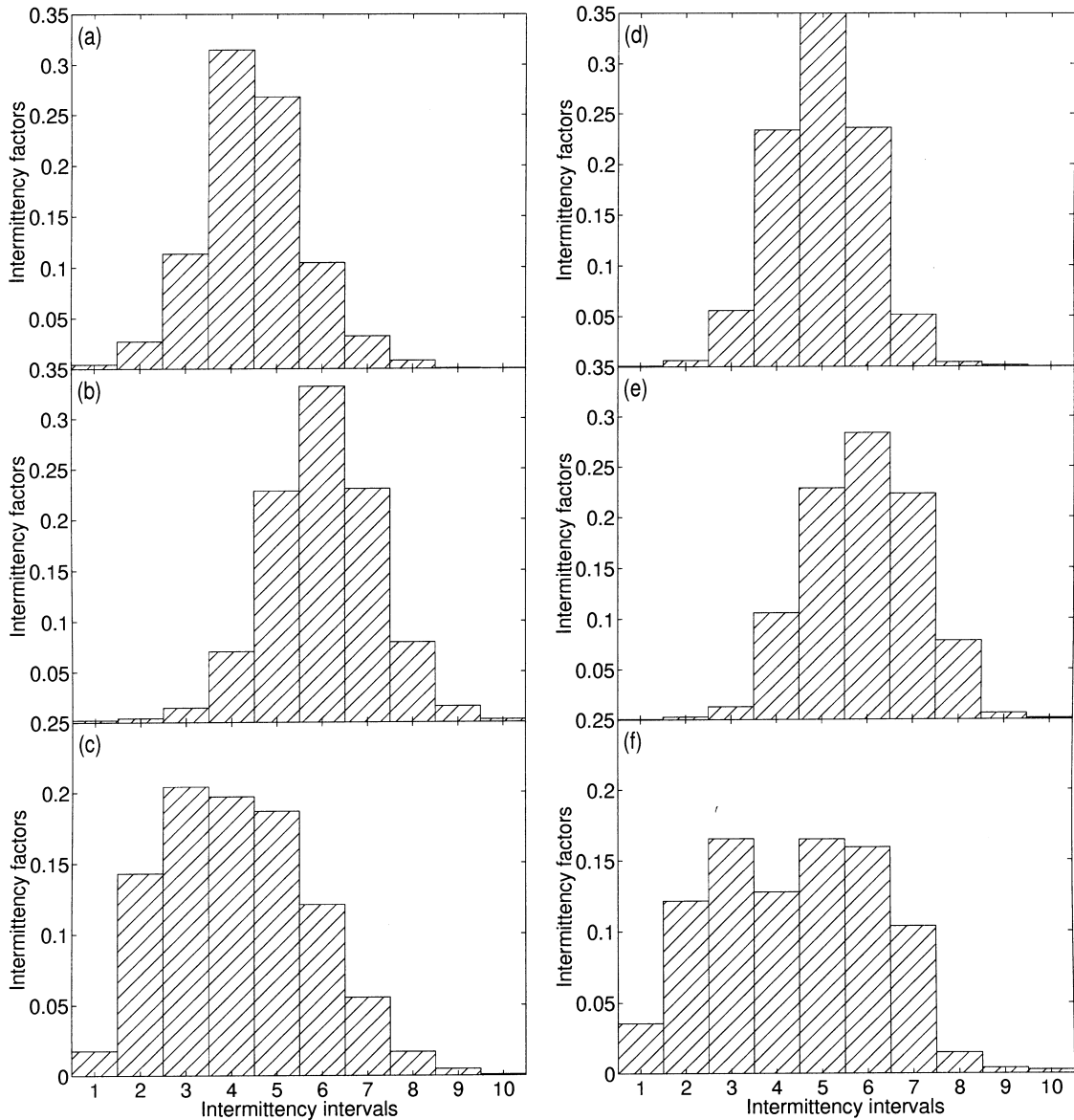
Fig. 5. Intermittency distributions of the experimental time series at different axial locations along the flame: (a) $h = 0.5$ cm, (b) $h = 4.0$ cm and (c) $h = 7.0$ cm. Intermittency distributions of the time series obtained from the best fit combinations of logistic maps: (d) $h = 0.5$ cm, (e) $h = 4.0$ cm and (f) $h = 7.0$ cm.

2(a–c)), indicates that as we go higher in the flame, the prevailing turbulent field exerts a greater influence on the fluctuations of soot volume fraction; and consequently, there is a progressive weakening of the influence of past history.

The search procedure produced $Q_{min} \sim \mathcal{O}(10^{-6})$ for all three locations in the flame considered here. To put this into context, we note that the maximum value was

$Q_{max} \sim \mathcal{O}(10^{-2})$, The time series for the best cases are shown in Fig. 2(d–f); the corresponding power spectra and delay maps (delay = 4) are shown in Fig. 3(d–f) and 4(d–f), respectively, and the histograms of the intermittency distributions are presented in Fig. 5(d–f). These results have to be compared with the experimental data, Figs 2(a–c), 3(a–c), 4(a–c) and 5(a–c), respectively. The quantitative values for the various statistical properties

Table 2
Map parameters corresponding to the best data fits for different
locations along the flame

Map, k	α_k	b_k	ω_k	d_k
(a)				
$\theta = 0.110$				
1	2.350 [0]	-3.82260	2000	200
2	1.500 [0]	-3.93864	170	158
3	$-6.310\,[-1]$	-4.00956	1	1
4	$2.000\,[-1]$	-4.13440	1	1
(b)				
$\theta = 0.277$				
1	2.282 [1]	-3.82260	2000	90
2	9.050 [0]	-3.93864	170	158
3	-1.700 [1]	-4.00956	1	1
4	-1.800 [0]	-4.13440	1	1
(c)				
$\theta = 0.320$				
1	4.198 [1]	-3.82260	2000	90
2	2.900 [0]	-3.93864	170	158
3	-4.420 [1]	-4.00956	1	1
4	2.000 [0]	-4.13440	1	1

(a) $h = 0.5$ cm, (b) $h = 4.0$ cm and (c) $h = 7.0$ cm.

discussed earlier are presented in Table 1 for both the modeled and experimental data at the $h = 4.0$ cm location. Similar tables can be constructed for the other locations but are not presented here.

From the experience gained during this research, it appeared that the autocorrelations were not important in obtaining a good match between modeled and computed data in the present case; hence, these were ultimately removed from the analysis. The skewness and flatness properties also produced only a minor contribution to the fitting process. However, it was found that the intermittency factors were critical for a good data fit. The normalized weights shown in the fifth column of table 1 reflect this, with smaller weights assigned to skewness and flatness while the intermittency factors are heavily weighted. The algorithm used to specify the weights was designed such that every important property had a balanced contribution to Q. In particular, the raw weights $\bar{\phi}_i$, were specified as

$$\bar{\phi}_i = \begin{cases} 1.0 & \text{for } i = 1,\ldots,21 \\ 0.1 & \text{for } i = 22, 23 \text{ (skewness and flatness)}, \\ \dfrac{1}{(p_i^{\text{meas}})^2} & \text{for } i = 24,\ldots,33 \text{ (intermittencies)}, \end{cases}$$

(18)

and the normalized weights ϕ_i, were computed from these by

$$\phi_i = \frac{\bar{\phi}_i}{\sum\limits_{i=1}^{Np} \bar{\phi}_i}.$$

The time series, (Figs 2(a–c) and 2(d–f)), are in reasonably good qualitative agreement in the sense that corresponding figures have similar qualitative appearance. (One would not expect pointwise detailed agreement for turbulent behavior.) From these figures it can be seen that the time averages and the amplitudes and frequency of oscillations match very well and follow the correct trends along the flame axis. The different scales of 'structures' are replicated in detail in the modeled time series. The distinct amplitudes α_k in Table 2 give quantitative information about the relative sizes of the different scales. There is generally good quantitative agreement too, as can be seen from Table 1.

The agreement in the power spectra, Fig. 3, is quite striking particularly because these were not part of the modeling process. Apart from the fairly good agreement in the overall power levels and decay rates, it can be seen that the model is able to replicate the sub-harmonic bifurcation indicated by the 6 and 12 Hz peaks. The experimental data show a sharp peak at 10.8 Hz (probably due to quasi-periodicity); the model is able to replicate this at the correct power but at a frequency of 10 Hz. This may be an inherent limitation of the logistic map in producing quasi-periodic bifurcations. The delay maps in Fig. 4, appear to be topologically equivalent. The delay map for the modeled time series at $h = 7.0$ cm location, Fig. 4(f), has at least two points where the trajectories are clustered together which is indicative of an underlying periodic behavior. A hint of this behavior can also be seen in the corresponding experimental delay map, Fig. 4(c), where we can see trajectories loosely clustered into two separate lobes.

The skewness in the experimental intermittency distribution, Fig. 5(a–c), changes along the flame. The same general behavior is also observed in the intermittency distribution of the model, Fig. 5(d–f). But there are some differences in the details, e.g., the intermittency distribution in the modeled case shown in Fig. 5(d) is more symmetric than the distribution in the corresponding experimental case shown in Fig. 5(a). One probable cause for this is the weights associated with $u_{\min}$ and $u_{\max}$. These properties are a part of the fitting procedure and influence the intermittency calculations because they determine the end points, g_0 and g_M, in equation (14). If these properties are not matched closely between experimental and modeled data then this would imply that the intermittency calculations are being done in slightly different intervals in the two cases, leading to the differences observed in Fig. 5(a, d). The remedy to this is to match $u_{\min}$ and $u_{\max}$ very closely for experimental and modeled data by using

greater weights on these properties. This will be implemented in future research involving the present data fitting approach.

4.2. Predictions from maps with interpolated parameters

As discussed earlier, here we will attempt to predict the time series and their quantifying measures at intermediate locations in the flame with the map parameters obtained by interpolation of the parameters calculated by data-fitting in the previous section. Experimental time series at two intermediate locations ($h = 2.0$ cm and $h = 6.0$ cm) are available and are shown in Fig. 6(a, b). These will be used to compare the predictions from the interpolated maps.

We use a quadratic polynomial interpolation to obtain the parameters of the map combination at the intermediate locations. It should be noted from Table 2 that some parameters which are constant for all the locations (including all the b_k values) are not interpolated. Interpolation is done for all the amplitudes, α_k, ad the duration count, d_1, that change with location. It can be seen from

Table 2 that parameters like α_1 and α_3 are monotonically increasing (or decreasing), and reasonable results can be expected by interpolation of these parameters. Other parameters like α_2 and α_4 vary quite nonlinearly (maybe chaotically) and it is not clear what a good interpolating function for these ought to be. Here we use quadratic interpolation for simplicity and for the lack of any physical reasons for doing otherwise. The interpolated set of map parameters are shown in Table 3 for $h = 2.0$ cm and $h = 6.0$ cm locations, respectively. The map time series obtained for these parameters are shown in Fig. 6(c, d). As was done before, we generate psds and intermittency histograms for both the experimental data (shown in Figs 7(a, b) and 8(a, b)) and also for data from the interpolated maps (shown in Figs 7(c, d) and 8(c, d)). We compute the statistical properties and the least-squares functional, Q, which are shown in Table 4 for only the $h = 2.0$ cm axial location.

Despite the fact that we are attempting the difficult task of trying to predict the behavior of a highly nonlinear system, the experimental data, with another simpler nonlinear system, the chaotic map combination, the quali-
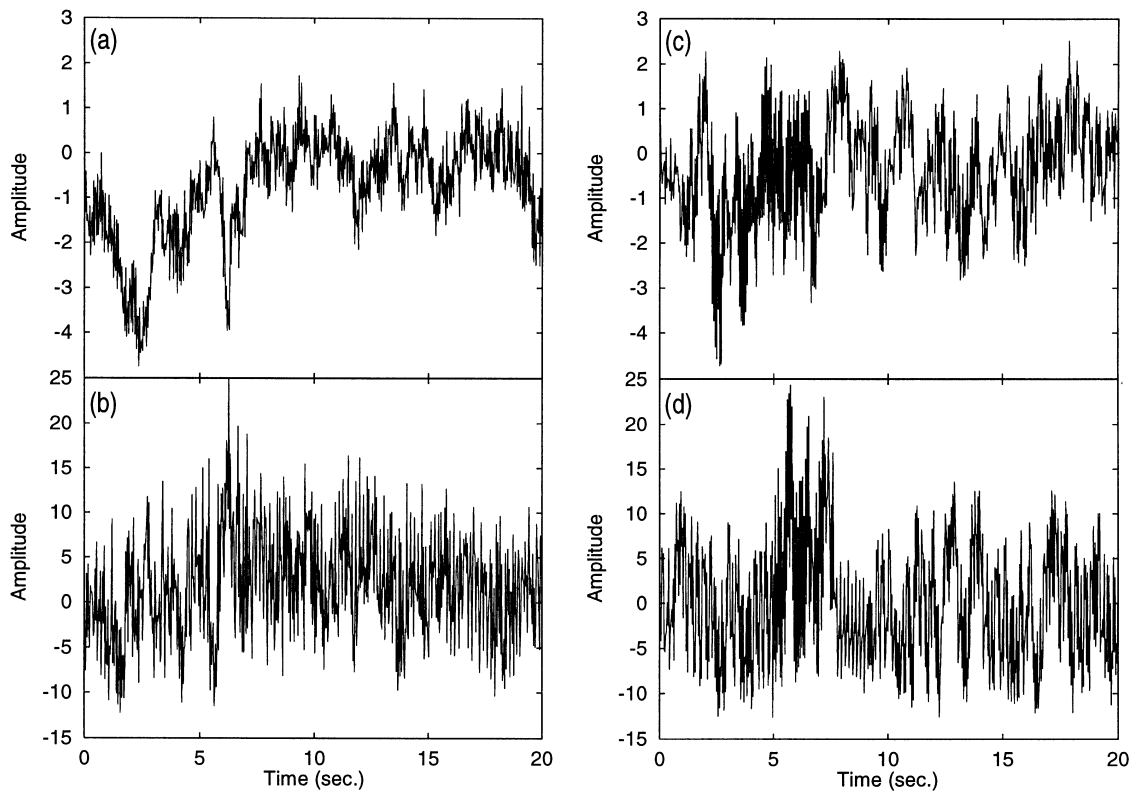

Fig. 6. Experimental time series of light scattering intensities at two intermediate locations along the flame: (a) $h = 2.0$ cm and (b) $h = 6.0$ cm. Corresponding predicted time series obtained from linear combination of logistic maps with interpolated parameters: (c) $h = 2.0$ cm and (d) $h = 6.0$ cm.

Table 3
Map parameters obtained by quadratic interpolation of those of Table 2 for intermediate locations along the flame

Map, k	α_k	b_k	ω_k	d_k
(a)				
$\theta = 0.197$				
1	1.087 [1]	−3.82260	2000	138
2	6.677 [0]	−3.93864	170	158
3	−5.620 [0]	−4.00956	1	1
4	−1.505 [0]	−4.13440	1	1
(b)				
$\theta = 0.316$				
1	3.543 [1]	−3.82260	2000	80
2	6.245 [0]	−3.93864	170	158
3	−3.378 [1]	−4.00956	1	1
4	1.719 [0]	−4.13440	1	1

(a) $h = 2.0$ cm, (b) $h = 6.0$ cm

tative agreement in the time series, Fig. 6(a–d), is fairly good in terms of mean values, amplitudes and oscillation frequencies. It can be seen from Table 4, that although the quantitative agreement between predicted and measured statistics is good, the functional, Q, obtained from the maps with the interpolated parameters is an order of magnitude larger than that obtained by data-fitted maps. This is to be expected because the quadratic fit is only a convenient approximation that is used here to interpolate map parameters some of which vary in a nonlinear fashion for different locations on the flame. It can be seen that the power spectra, Fig. 7(a–d), also agree well not only in terms of the gross features like overall power levels and decay rates, but also in the finer details of the subharmonic and quasiperiodic peaks. The overall match in intermittency factors, Fig. 8(a–d), is not very good although they roughly show the correct skewness in oscillatory data. The peaks in the intermittency data from the experimental time series are not reproduced in the
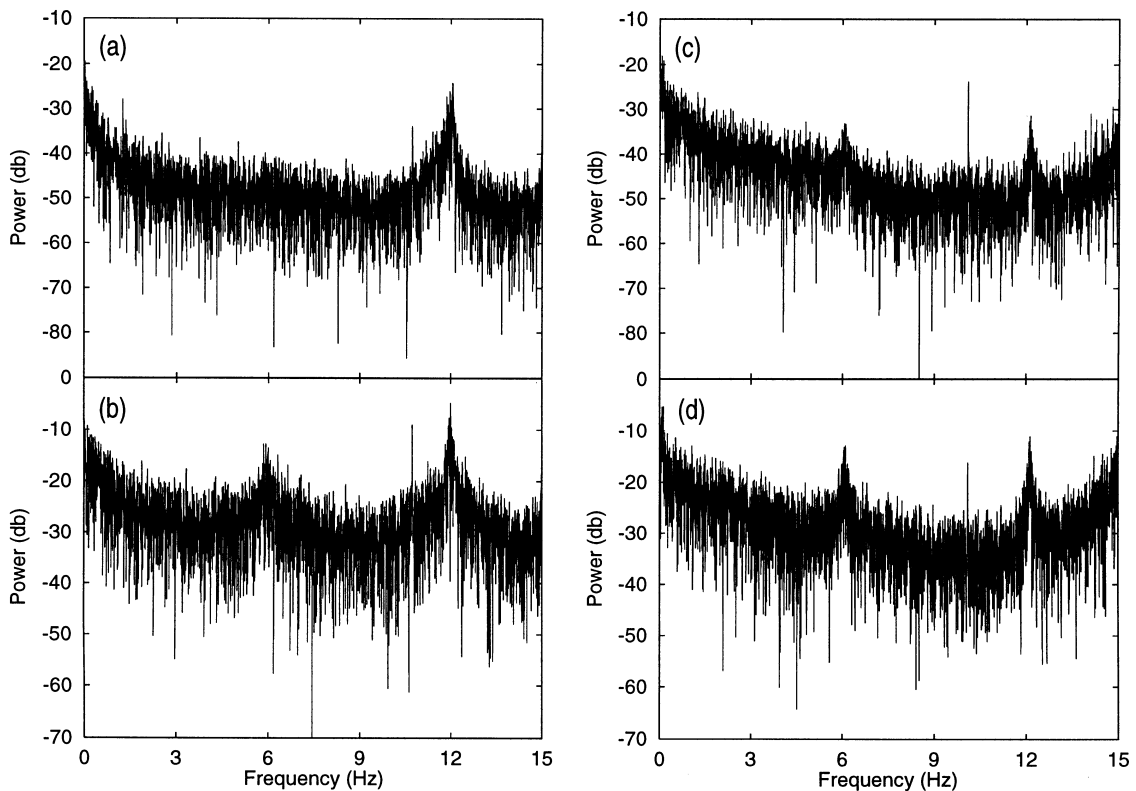

Fig. 7. Power spectra from experimental time series of soot scattering intensity at intermediate locations: (a) $h = 2.0$ cm, and (b) $h = 6.0$ cm along the flame. Corresponding power spectra of time series obtained from a combination of logistic maps with interpolated parameters: (c) $h = 2.0$ cm and (d) $h = 6.0$ cm.
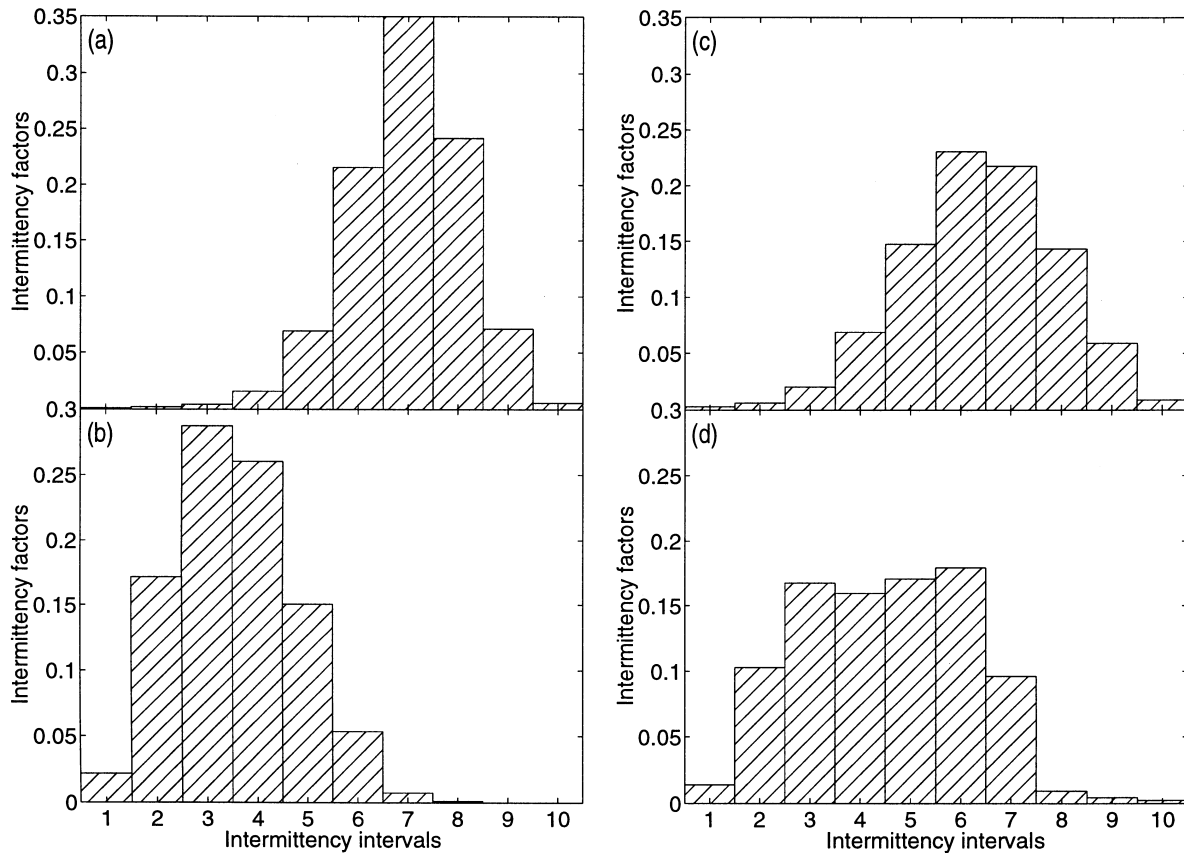
Fig. 8. Intermittency distributions of the experimental time series at intermediate locations: (a) $h = 2.0$ cm and (b) $h = 6.0$ cm, along the flame. Intermittency distributions of the time series obtained from a combination of interpolated logistic maps: (c) $h = 2.0$ cm and (d) $h = 6.0$ cm.

predicted data from the chaotic map models. This only emphasizes our previous observation from the data-fitting exercise that the intermittency factors are important in obtaining a good match between the two time series. A close match between intermittency factors cannot be guaranteed without resorting to a data-fitting procedure.

5. Summary and conclusions

In this paper we have discussed a novel approach to investigate the radiation–turbulence interactions in diffusion flames. We have modeled experimental data from a soot-laden turbulent diffusion flame produced with a co-flow burner. The data show strong evidence of a subharmonic bifurcation sequence from periodic behavior at the tip of the burner to fully turbulent at some height (depending on air/fuel ratio) above the burner.

On the basis of these observations we have constructed chaotic map models of this behavior using linear combinations of a modified logistic map.

We can draw several conclusions from this study that we hope may lead to innovations in turbulence modeling approaches:

• The radiation–turbulence interaction phenomenon in a soot-laden flame is evidently deterministic, rather than random, as has been reported earlier [1].

• It is possible to devise fairly simple algebraic models of this quite complicated flow situation, but unlike earlier attempts with other physical systems, our model displays correct bifurcation sequences in addition to accurate behavior at individual parameter settings within the sequence. This implies a potential for 'universality' and indicates that such models should be extremely useful in the context of the ATD/chaotic map turbulence modeling formalism as well as possibly in LES.

Table 4
Statistical properties of data from experiments and predictions from chaotic map model with interpolated parameters for location $h = 2.0$ cm in the flame

Property no. i	Description	Measured value p_i^{meas}	Modeled value p_i^{model}	Weights ϕ_i	Contribution to Q $\phi_i(\delta p_i)^2$
1	Average ($\bar{u}$)	-8.731 [-4]	-3.923 [-1]	8.756 [-7]	1.341 [-7]
2	Positive average ($\bar{u}^+$)	6.243 [-1]	8.149 [-1]	8.756 [-7]	3.182 [-8]
3	Negative average ($\bar{u}^-$)	-6.811 [-1]	-1.150 [0]	8.756 [-7]	1.929 [-7]
4	Average variation ($\bar{V}(u)$)	7.208 [-1]	1.059 [0]	8.756 [-1]	1.002 [-7]
5	Positive average variation ($\bar{V}^+(u)$)	5.927 [-1]	7.117 [-1]	8.756 [-7]	1.239 [-8]
6	Negative average variation ($\bar{V}^-(u)$)	6.097 [-1]	9.428 [-1]	8.756 [-7]	9.717 [-8]
7	Slope sign changes, total ($f_{s\pm}$)	7.747 [-1]	7.810 [-1]	8.756 [-7]	3.477 [-11]
8	Slope sign changes, u positive ($f_{s\pm}^+$)	7.685 [-1]	7.848 [-1]	8.756 [-7]	2.322 [-10]
9	Slope sign changes, u negative ($f_{s\pm}^-$)	7.813 [-1]	7.785 [-1]	8.756 [-7]	6.819 [-12]
10	Time average L^1 norm	6.514 [-1]	1.021 [0]	8.756 [-1]	1.195 [-7]
11	Time average L^2 norm	4.609 [-2]	7.062 [-2]	8.756 [-7]	5.270 [-10]
12	Overall minimum (u_{min})	-4.741 [0]	-5.283 [0]	8.756 [-7]	2.569 [-7]
13	Overall maximum (u_{max})	2.587 [0]	3.031 [0]	8.756 [-7]	1.726 [-7]
14	Positive minimum (u_{min}^+)	3.034 [-4]	1.211 [-3]	8.756 [-7]	7.219 [-13]
15	Positive maximum (u_{max}^+)	2.587 [0]	3.031 [0]	8.756 [-7]	1.726 [-7]
16	Negative minimum (u_{min}^-)	-4.741 [0]	-5.283 [0]	8.756 [-7]	2.569 [-7]
17	Negative maximum (u_{max}^-)	0.000 [0]	0.000 [0]	8.756 [-7]	0.000 [0]
18	Number of zero crossings/time (N_0/N)	3.801 [-1]	3.259 [-7]	8.756 [-7]	2.573 [-9]
19	Number of $\bar{u}$ crossings/time (N_{mean}/N)	3.801 [-1]	3.481 [-1]	8.756 [-7]	8.970 [-10]
20	Number of $\bar{u}^+$ crossings/time (N_{mean^+}/N)	3.065 [-1]	2.223 [-1]	8.756 [-7]	6.195 [-9]
21	Number of $\bar{u}^-$ crossings/time (N_{mean^-}/N)	2.124 [-1]	2.897 [-1]	8.756 [-7]	5.220 [-9]
22	Skewness	-5.625 [-1]	-1.097 [0]	8.756 [-8]	2.506 [-8]
23	Flatness	4.414 [0]	3.362 [0]	8.756 [-8]	9.677 [-8]
24	Intermittency factor (f_{I_1})			7.233 [-1]	2.345 [-6]
25	Intermittency factor (f_{I_2})			1.985 [-1]	3.177 [-6]
26	Intermittency factor (f_{I_3})	Inter-	Inter-	4.734 [-2]	1.227 [-5]
27	Intermittency factor (f_{I_4})	mittency	mittency	3.506 [-3]	9.890 [-6]
28	Intermittency factor (f_{I_5})	factors	factors	1.822 [-4]	1.112 [-6]
29	Intermittency factor (f_{I_6})	shown	shown	1.886 [-5]	4.303 [-9]
30	Intermittency factor (f_{I_7})	graphically	graphically	7.096 [-6]	1.269 [-7]
31	Intermittency factor (f_{I_8})	in Fig. 8(a)	in Fig. 8(c)	1.498 [-5]	1.445 [-7]
32	Intermittency factor (f_{I_9})			1.722 [-4]	2.564 [-8]
33	Intermittency factor ($f_{I_{10}}$)			2.694 [-2]	2.760 [-7]

Least-squares functional, $Q = 3.106$ [-5]. Maximum contribution to Q is from property 26, f_{I_3}.

References

[1] M.P. Mengüç, J.M. McDonough, S. Manickavasagam, S. Mukerji, S. Swabb and S. Ghosal, Fluctuations of soot in turbulent diffusion flames: Experimental data and chaotic map models. Presented at ASME International Mechanical Engineering Congress and Exposition, Atlanta, GA, November 1996, pp. 17–22.

[2] G.M. Faeth, S.M. Jeng, J. Gore, Radiation from flames, in: C.K. Law, et al. (Eds.), Heat transfer in fire and combustion systems, HTD-Vole 45, ASME, New York.

[3] W.L. Grosshandler, P. Joulain, The effect of large scale fluctuations on flame radiation, in: Progress in astronautics and aeronautics, Vol. 105, Part II. AIAA, Washington, 1986, pp. 123–152.

[4] J.P. Gore, S.M. Jeng, G.M. Faeth, Spectral and total radiation properties of turbulent hydrogen/air diffusion flames. ASME Journal of Heat Transfer 110 (1988) 173–181.

[5] G.M. Faeth, J.P. Gore, S.G. Chuech, S.M. Jeng, Radiation from turbulent diffusion flames, in: C.L. Tien, T.C. Chawla (Eds.), Annual review of numerical fluid mechanics and heat transfer, Hemisphere, New York, 1989, pp. 1–38.

[6] M.E. Kounalakis, Y.R. Sivathanu, G.M. Faeth, Infrared radiation statistics of nonluminous turbulent diffusion flames, ASME Journal of Heat Transfer 113 (1991) 437–445.

[7] Y.R. Sivathanu, J.P. Gore, Coupled radiation and soot kinetics calculations in laminar acetylene/air diffusion flames, Combustion and Flame 97 (1994) 161–172.

[8] C.J. Freitas, Perspective: Selected benchmarks from commercial CFD codes, Journal of Fluids Engineering 117 (1995) 208–218.

[9] J.M. McDonough, On intrinsic errors in turbulence models based on Reynolds-averaged Navier–Stokes equations, Fluid Mechanics Research 22 (1995) 1–29.

[10] E.C. Hylin, J.M. McDonough, Theoretical development of a stochastic model for small-scale turbulence in an additive decomposition of the Navier–Stokes equations, Mechanical Engineering report CFD-02-96, University of Kentucky, Lexington, KY, 1996.

[11] K.R. Sreenivisan, R. Ramshankar, Transition intermittency in open flows, and intermittency routes to chaos, Physica, 23D (1986) 246–258.

[12] J.M. McDonough, S. Mukerji, S. Chung, A data-fitting procedure for chaotic time series, to appear in Applied Mathematics and Computation (1998).

[13] P. Collet, J.-P. Eckmann, Iterated maps on the interval as dynamical systems, Birkhäuser–Boston, Boston, 1980.

[14] M.J. Feigenbaum, Quantitative universality for a class of nonlinear transformations, Journal of Statistical Physics 19 (1978) 25–52.

[15] T.H. Pulliam, J.A. Vastano, Transition to chaos in an open unforced 2D flow, Journal of Computational Physics, 105 (1993) 133–149.

[16] U. Frisch, Turbulence, Cambridge University Press, Cambridge, 1995.

[17] J.M. McDonough, R.J. Bywater, J.C. Buell, An investigation of strange attractor theory and small-scale turbulence, AIAA Paper 84–1674, 1984.

[18] J.M. McDonough, J.C. Buell, R.J. Bywater, A comparison of routes to a strange attractor in one-dimensional local models of turbulent free and forced convection, ASME Paper 84-WA/HT-16, 1984.

[19] J.M. McDonough, R.J. Bywater, Large-scale effects on local small-scale chaotic solutions to Burgers' equation, AIAA Journal 24 (1986) 1924–1930.

[20] J.M. McDonough, R.J. Bywater, Turbulent solutions from an unaveraged additive decomposition of Burgers' equation, in: W.W. Bower, M.J. Morris (Eds.), Forum on turbulent flows, American Society of Mechanical Engineers (ASME), 1989, pp. 7–12.

[21] J.M. McDonough, D. Wang, Additive turbulent decomposition: a highly parelizable turbulence simulation technique, in: N. Satufoka, et al. (Eds.), Parallel computational fluid dynamics: new algorithms and applications, Elsevier Science B.V., Amsterdam, 1995, 129–136.

[22] S. Mukerji, J.M. McDonough, Parallel computation of 3-D small scale turbulence via additive turbulent decomposition, in: A. Acer, et al. (Eds.), Parallel computational fluid dynamics: Implementations and results using parallel computers, Elsevier Science B.V., Amsterdam, 1996, pp. 465–472.

[23] J.M. McDonough, Y. Yang, E.C. Hylin, Modeling time-dependent turbulent flow over a backward-facing step via additive turbulent decomposition and chaotic algebraic maps, in: W.H. Hui, Y.-K. Kwok, J.R. Chasnov, Proceedings of the First Asian Computational Fluid Dynamics Conference, 1995, pp. 747–752.

[24] J.M. McDonough, D. Wang, M.P. Mengüç, Radiation–turbulence interaction in flames using additive turbulent decomposition. In: M.P. Mengüç, Radiative Transfer—I: Proceedings of the First International Symposium on Radiative Transfer. Begell House, New York, 1996.

[25] A.J. Salazar, J.M. McDonough, S. Mukerji, Transient heat transfer and fluid flow over an internal turbulence promoter via ATD/chaotic-map modeling, ASME Paper FEDSM97-3166, 1997.

[26] M. Marion, R. Temam, Nonlinear Galerkin methods, SIAM Journal on Numerical Analysis 26 (1989) 1139–1157.

[27] R.M. Brown, P. Perry, Z. Shen, The additive turbulent decomposition for the two-dimensional incompressible Navier–Stokes equations: convergence theorems and error estimates, to appear in SIAM Journal of Mathematical Analysis, 1998.

[28] D.C. Wilcox, Turbulent modeling for CFD, DCW Industries, Inc., La Cañada, CA, 1993.

[29] H. Tennekes, J.L. Lumley, A first course in turbulence, MIT Press, Cambridge, MA, 1973.

[30] J. Buckmaster, N. Peters, The infinite candle and its stability—a paradigm for flickering turbulent diffusion flames, Proceedings of the 21st International Symposium on Combustion, 1986, the Combustion Institute, Pittsburgh, PA, 1829–1936.

[31] D. Ruelle, F. Takens, On the nature of turbulence, Communications in Mathematical Physics 20 (1971) 167–192.

[32] J. Guckenheimer, P. Homes, Nonlinear oscillations, dynamical systems, and bifurcations of vector fields, Springer–Verlag, New York, 1983.

[33] P. Bergé, Y. Pomeau, C. Vidal, Order within chaos, John Wiley and Sons, New York, 1984.